International Journal of Heat and Technology
Vol. 44, No. 1, February, 2026, pp. 1-11
Journal homepage: http://iieta.org/journals/ijht

Optimizing Performance in PEM Fuel Cells: A Simulation Study of T-Junction Fractal Flow Field Plate

Abdelhakim Merdjani[1*], Natalia Kizilova[1], Tabbi Wilberforce Awotwe[2]

[1] Institute of Aeronautics and Applied Mechanics, Warsaw University of Technology, Warszawa 00-665, Poland
[2] Faculty of Natural, Mathematical and Engineering Sciences, King's College London, Strand, London WC2R 2LS, United Kingdom

Corresponding Author Email: abdelhakim.merdjani.dokt@pw.edu.pl

https://doi.org/10.18280/ijht.440101

Received: 1 November 2025
Revised: 9 December 2025
Accepted: 15 December 2025
Available online: 28 February 2026

Keywords:
proton exchange membrane fuel cell, computational fluid dynamics, bio-inspired fractal flow-field design, energy efficiency

ABSTRACT

This study presents a novel T-junction fractal flow field plate (FFP) for proton exchange membrane fuel cells (PEMFCs), designed according to Murray's law and an entropy-based scaling criterion. The concept introduces a reduced-thickness plate compared to existing fractal architectures, aiming to simplify manufacturing while enhancing reactant distribution and water management. A three-dimensional, non-isothermal, multiphase computational fluid dynamics (CFD) model is used to evaluate concentration fields, current density distribution, heat generation, and liquid water behaviour under varying relative humidity (RH) conditions. Simulation results indicate that the fractal design improves performance by 8% relative to a standard serpentine configuration with the same 25 cm² active area, attributed to more uniform oxygen delivery and lower local entropy generation. The optimal operating condition is observed at 70% RH, where a balance between membrane hydration and liquid water removal is achieved: performance declines at higher RH due to local flooding. Based on water transport analysis, two strategies are proposed for further improvement: relocating outlets to facilitate drainage and incorporating microgrooves to support capillary removal. The findings highlight the potential of low-thickness fractal FFPs for high-efficiency and cost-effective PEMFC development.

1. INTRODUCTION

The application area of fuel cells (FCs) is rapidly expanding due to their ability to directly convert chemical energy into electrical energy with high efficiency and minimal environmental impact. Among various FC types, proton exchange membrane fuel cells (PEMFCs) have gained significant attention due to their wide range of applications, high energy density, and silent operation. PEMFCs are composed of several key components, including Bipolar Plates (BPs) with flow-field channels, membrane electrode assemblies (MEA) with catalyst layers (CL), and Gas Diffusion Layers (GDLs), as shown in Figure 1 [1-5]. These components play crucial roles in ensuring efficient electrochemical reactions and overall system performance.

Among these components, the design and material selection of the flow field plates (FFPs) have garnered increased interest from researchers, as they directly impact the FC's efficiency, durability, and cost-effectiveness. FFPs serve multiple functions, such as distributing reactant gases evenly across the MEA, facilitating product water removal, and assisting in thermal and electrical management. In fact, FFPs contribute approximately 60% of the overall FC weight and nearly 30% of the manufacturing cost [6, 7]. Therefore, optimizing FFP designs is crucial for improving PEMFC performance and achieving cost-effective commercialization [8-10]. Bio-inspired FFPs designs have emerged as promising alternatives to traditional configurations. These designs draw inspiration from natural structures that have evolved to optimize fluid distribution, such as tree branches, lung airways, and vascular networks. Fractal designs, as shown in Figure 2, in particular, have demonstrated superior gas distribution properties compared to conventional serpentine and parallel designs. By mimicking naturally efficient flow patterns, these bio-inspired structures can enhance PEMFC performance by ensuring uniform reactant distribution and reducing pressure losses. However, despite these advantages, fractal designs face challenges related to manufacturing complexity and water management, which can limit their practical implementation [11-13].

The present computational fluid dynamics (CFD) study addresses two key limitations of existing fractal FFP concepts: the manufacturing complexity and thickness of previously proposed tree-like plates, and the insufficient control of water management at high generations of fractal branching. To this end, a developed T-junction fractal FFP is designed for the cathode side of a 25 cm² PEMFC, based on Murray's law and an entropy-minimizing diameter scaling parameter. The proposed plate features a reduced thickness compared to reported fractal designs, thereby simplifying fabrication while preserving the uniform distribution network.

$$\text{Anode: } H_2 \rightarrow 2H^+ + 2e^-$$
$$\text{Cathode: } \frac{1}{2}O_2 + 2H^+ + 2e^- \rightarrow H_2O \quad (1)$$

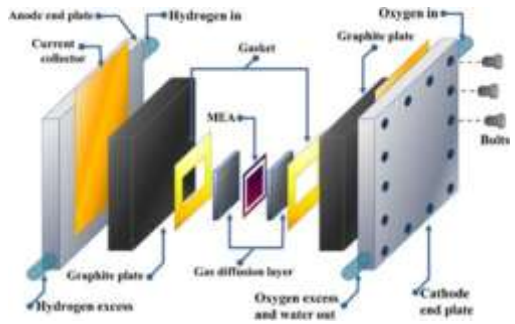

Figure 1. Schematic diagram showing the components of a single proton exchange membrane fuel cell (PEMFC) [5]

Based on the simulated water transport behaviour, two conceptual design modifications are also proposed: repositioning outlets to enhance drainage of liquid water and integrating microgrooves to promote capillary-driven removal from the GDL and channels. These propositions are intended as practical guidelines for future experimental implementation.

1.1 Flow-field design evaluation criteria

The evaluation of FFP designs in PEMFC involves several crucial criteria, including pressure drop, reaction uniformity, water management, and manufacturing complexity, as presented in Table 1. A minimized pressure drop is also essential to enhance energy efficiency by reducing the operational strain on pumps and compressors. Equally important is the uniform distribution of reactants across the catalytic surfaces to avoid gradual cell degradation. Effective water management within the FC is vital to maintain membrane hydration for optimal ionic conductivity while also preventing flooding that can impede GDL and MEA [14]. Lastly, the complexity of manufacturing FFPs significantly affects both the scalability and cost of the cell. All those influencing the operational stability and functionality of FC.

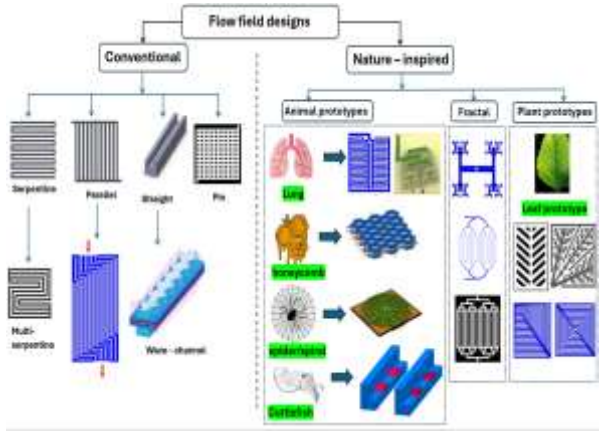

Figure 2. Bipolar plate designs in proton exchange membrane fuel cell (PEMFC)

Table 1. Evaluation of existing bio-inspired design of FFP; (+) are advantages, (-) are limitations, (n/a) are not mentioned

Flow Field Design	Pressure Drops	Gas Distribution Uniformity	Water Content	Manufacturing Complexity	Compared to Conventional FFP	Ref.
Novel Bionic Spider-Web-Type	+	+	n/a	+	> straight FFP < serpentine FFP	[15]
fishbone-shaped cathode	+	+	+	-	8.7% > parallel.	[16]
Novel bionic bird type	+	+	+	+	5.894% > serpentine.	[17]
Bionic leaf shaped (1)	+	-	n/a	+	n/a	[18]
Leaf shaped (2)	+	-	n/a	+	20–25% > serpentine	[19]
Leaf shaped (3)	+	-	n/a	+	26% > serpentine	[20]
Ginkgo shaped	+	-	n/a	-	7% < serpentine 40% > parallel	[21]
Lung shaped (1)	+	+	n/a	-	> serpentine > parallel	[22]
Lung shaped (2)	+	+	n/a	-	14% to 41% > serpentine.	[23]
Lung shaped (3)	-	+	-	-	25% > serpentine.	[24]
Lung shaped (4)	-	-	n/a	+	n/a	[25]
Topology optimization	+	-	n/a	-	5.7% > parallel.	[26]
Tree shaped (1)	+	+	n/a	+	33.5% < serpentine 50% > parallel	[27]
Tree shaped (2)	+	+	-	-	11% < serpentine	[28]
Leaf and tree shaped	-	-	n/a	+	5.12% > serpentine	[29]
Spiral shaped	-	-	+	+	11.9% > serpentine	[30]
Spiral-nautilus shaped	-	+	n/a	-	21.53% > serpentine	[31]
Superior mesenteric branch shaped	-	+	n/a	-	3.16% < serpentine	[32]
Superior mesenteric branch shaped	-	+	n/a	-	25% > parallel	[33]

1.2 Theory of bio-inspired designs

The bio-inspired designs are mostly based on Murray's law, which was discovered on the bifurcations of arterial blood vessels and airways in animals and humans [34, 35]. Later, it was detected in the construction of the fluid flow passages in plants [36], sponges, and fish [37]. The law states that the diameters of the parent branch d_0 and its daughter branches d_1, d_2, …, d_n satisfy the relationship.

$$d_0^{\gamma} = d_1^{\gamma} + d_2^{\gamma} + \cdots + d_n^{\gamma} \quad (2)$$

where, γ = 3 for laminar flows, and γ = 7/3 for turbulent flows [38].

In this study, the fractal T-junction design of the FFP is considered based on (2) and on the impact of the total entropy production in the FFP. The value of 0.794 for the dimensionless diameter scaling parameter provided the lowest total entropy production for the FFP geometry [39].

1.3 Fractal design of flow field plate in PEMFC

Fractal binary tree patterns represent innovative design approaches for FFP, which are based on human lungs or vein networks of plant leaves. Sauermoser et al. [28] investigated the T-junction fractal FFP. The study focused on the development and testing of a new FFP design with varying width-scaling parameters, aiming to achieve a uniform distribution of reactants and improve the performance of PEMFCs. The tree-like FFP designs were CNC milled on high-quality graphite plates, and three designs with different width-scaling parameters were employed in the experimental investigations. It was noted that the RH had no significant impact on the FC performance and electrochemical impedance spectroscopy test of the classical serpentine FFP, indicating proper membrane hydration. However, for the tree-like FFP, higher charge transfer resistances and Warburg diffusion impedances were observed at even low RH, indicating problems caused by poor water management.

Bethapudi et al. [40] used fractal FFP of a novel method of 3D flow field by using 2D planar printed circuit board plates with a layer-wise assembly approach. This design emulates the efficient, scalable air transport inside the lungs, a n-generation hierarchical fractal structure, with the airflow occurring from a single inlet to 2n-1 outlets.

Table 2. Summary of T-junction fractal FFPs

Parameters	Sauermoser et al. [28]	Bethapudi et al. [40]	Proposed Prototype (Current Study)
Number of outlets	128	1024	64
Thickness	5 mm (2 compressed plates)	< 5 mm (one plate for each generation)	3 mm
Width scaling	0.97	1	0.79
Outlet section-configuration	fractal	parallel	parallel

Despite the progress achieved in recent fractal-based PEMFC flow fields, important limitations remain. The work of Sauermoser et al. [28] demonstrated that channel width-scaling strongly affects performance, yet the optimal scaling factor and nominal number of fractal generations required for balanced reactant distribution and water removal were not fully established. Conversely, the multilayer fractal configuration proposed by Bethapudi et al. [40] enabled high outlet multiplicity and efficient transport, but its printed-circuit architecture increases fabrication complexity and is less compatible with low-cost industrial plate manufacturing. achieving a fractal flow field that combines optimal geometric scaling, controlled outlet generation, and practical manufacturability, while simultaneously improving water management. To address this, the present work introduces a reduced-thickness T-junction fractal FFP, designed using an entropy-informed scaling parameter and evaluated across multiple humidity conditions. The comparison in Table 2 summarizes how the proposed design positions itself relative to existing approaches in terms of generation count, scaling factor, thickness, and outlet configuration.

2. NUMERICAL MODELLING AND METHOD

A numerical study refers to the use of CFD modelling to simulate and analyse the behaviour of the proposed fractal FFP prototype, as shown in Figure 3. This study is conducted using a 3D multiphase model. This simulation was carried out by ANSYS FLUENT 2021 R1 software.

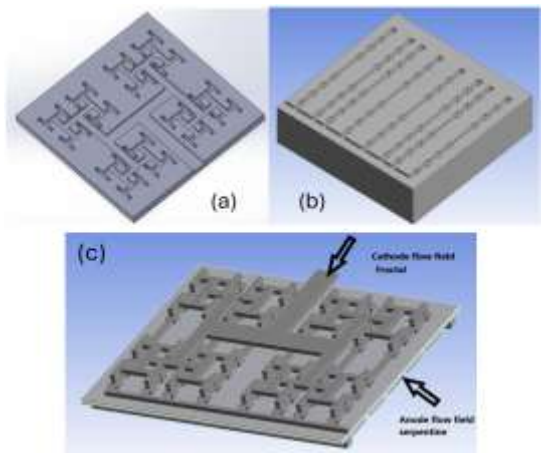

Figure 3. T-junction fractal FFP: (a) distributing system, (b) outlets, and (c) the entire cell

The PEMFC module is an add-on module of ANSYS FLUENT with capabilities of modelling electrochemical reactions, transport of protonic, ionic, and species gases, generation of water, heat, and electric energy [41]. The principal assumptions that are made in the module for the current study are:

- The operation of PEMFC is under steady-state conditions.
- Laminar flow of the reactants.
- Non-isothermal operation.
- Production and transportation of liquid water.
- Materials used for PEMFC are assumed to be by default.

2.1 Governing equations

According to the model description, the governing equations and associated source terms are expressed as follows [8, 41-43].

- Continuity equation:

$$\frac{\partial(\rho u)}{\partial x}+\frac{\partial(\rho v)}{\partial y}+\frac{\partial(\rho w)}{\partial z}=S_m \tag{3}$$

ρ [kg/m^3] is the fluid density. In the context of a PEMFC, it could represent the density of the reactant gas, such as hydrogen or oxygen.

u, v, w [m/s] are the velocity components in the x, y, and z directions, respectively. They describe the flow of the gas within the cell along each spatial axis.

S_m [kg/m^3·s] is the mass source term determined by chemical reactions.

• Momentum equation:

$$\begin{aligned} &u\frac{\partial(\rho u)}{\partial x}+v\frac{\partial(\rho u)}{\partial y}+w\frac{\partial(\rho u)}{\partial z}= \\ &-\frac{\partial P}{\partial x}+\frac{\partial}{\partial x}\left(\mu\frac{\partial u}{\partial x}\right)+\frac{\partial}{\partial y}\left(\mu\frac{\partial u}{\partial y}\right)+\frac{\partial}{\partial z}\left(\mu\frac{\partial u}{\partial z}\right)+S_{px} \\ &u\frac{\partial(\rho v)}{\partial x}+v\frac{\partial(\rho v)}{\partial y}+w\frac{\partial(\rho v)}{\partial z}= \\ &-\frac{\partial P}{\partial y}+\frac{\partial}{\partial x}\left(\mu\frac{\partial v}{\partial x}\right)+\frac{\partial}{\partial y}\left(\mu\frac{\partial v}{\partial y}\right)+\frac{\partial}{\partial z}\left(\mu\frac{\partial v}{\partial z}\right)+S_{py} \\ &u\frac{\partial(\rho w)}{\partial x}+v\frac{\partial(\rho w)}{\partial y}+w\frac{\partial(\rho w)}{\partial z}= \\ &-\frac{\partial P}{\partial z}+\frac{\partial}{\partial x}\left(\mu\frac{\partial w}{\partial x}\right)+\frac{\partial}{\partial y}\left(\mu\frac{\partial w}{\partial y}\right)+\frac{\partial}{\partial z}\left(\mu\frac{\partial w}{\partial z}\right)+S_{pz} \end{aligned} \tag{4}$$

P [Pa] is the operating pressure within the system.

μ [Pa·s] is the dynamic viscosity of the fluid, which accounts for the internal resistance to flow within the gas.

S_{px}, S_{py}, S_{pz} represent source terms in the x, y, and z projections of momentum equations. These terms account for body forces, such as gravity, and reaction forces inside the system.

• Energy

$$\begin{aligned} &u\frac{\partial(\rho CpT)}{\partial x}+v\frac{\partial(\rho CpT)}{\partial y}+w\frac{\partial(\rho CpT)}{\partial z}= \\ &\frac{\partial}{\partial x}\left(k\frac{\partial T}{\partial x}\right)+\frac{\partial}{\partial y}\left(k\frac{\partial T}{\partial y}\right)+\frac{\partial}{\partial z}\left(k\frac{\partial T}{\partial z}\right)+S_h \end{aligned} \tag{5}$$

Cp [J/(kg·K)] is the specific heat at Constant Pressure, which is the amount of heat required to raise the temperature.

T [K] is the operating temperature of the system.

k [W/m·K] is the thermal conductivity of the used material.

Sh [W/m^3] is the heat source term. This term represents internal heat generation or loss due to chemical reactions, phase changes, or other processes inside the system.

• Hydrogen transport (anode side)

$$\begin{aligned} &u\frac{\partial\left(\rho Y_{H_2}\right)}{\partial x}+v\frac{\partial\left(\rho Y_{H_2}\right)}{\partial y}+w\frac{\partial\left(\rho Y_{H_2}\right)}{\partial z}= \\ &\frac{\partial\left(J_{x,H_2}\right)}{\partial x}+\frac{\partial\left(J_{y,H_2}\right)}{\partial y}+\frac{\partial\left(J_{z,H_2}\right)}{\partial z}+S_{H_2} \end{aligned} \tag{6}$$

Y_{H2} is the mass fraction of hydrogen.

J_{H2} [kg/m^2·S] represents the flux of hydrogen; it describes the rate of hydrogen transport.

S_{H2} [kg/m^3·S] source term for hydrogen consumption at anode.

• Water transport (anode side)

$$\begin{aligned} &u\frac{\partial\left(\rho Y_{aw}\right)}{\partial x}+v\frac{\partial\left(\rho Y_{aw}\right)}{\partial y}+w\frac{\partial\left(\rho Y_{aw}\right)}{\partial z}= \\ &\frac{\partial\left(J_{x,aw}\right)}{\partial x}+\frac{\partial\left(J_{y,aw}\right)}{\partial y}+\frac{\partial\left(J_{z,aw}\right)}{\partial z}+S_{aw} \end{aligned} \tag{7}$$

ρ is water density.

Y_{aw} is the mass fraction of water at the anode side.

J_{aw} represents the flux of water.

S_{aw} [kg/m·s] source term for water vapour generation.

• Oxygen transport (cathode side)

$$\begin{aligned} &u\frac{\partial\left(\rho Y_{O_2}\right)}{\partial x}+v\frac{\partial\left(\rho Y_{O_2}\right)}{\partial y}+w\frac{\partial\left(\rho Y_{O_2}\right)}{\partial z}= \\ &\frac{\partial\left(J_{x,O_2}\right)}{\partial x}+\frac{\partial\left(J_{y,O_2}\right)}{\partial y}+\frac{\partial\left(J_{z,O_2}\right)}{\partial z}+S_{O_2} \end{aligned} \tag{8}$$

ρ is oxygen density.

Y_{O2} is the mass fraction of oxygen at the cathode side.

J_{O2} represents the flux of oxygen at the cathode.

S_{O2} source term for oxygen consumption at the cathode.

• Water transport (cathode side)

$$\begin{aligned} &u\frac{\partial\left(\rho Y_{cw}\right)}{\partial x}+v\frac{\partial\left(\rho Y_{cw}\right)}{\partial y}+w\frac{\partial\left(\rho Y_{cw}\right)}{\partial z}= \\ &\frac{\partial\left(J_{x,cw}\right)}{\partial x}+\frac{\partial\left(J_{y,cw}\right)}{\partial y}+\frac{\partial\left(J_{z,cw}\right)}{\partial z}+S_{cw} \end{aligned} \tag{9}$$

ρ is water density.

Y_{cw} is the mass fraction of water at the cathode side.

J_{cw} represents the flux of water at the cathode.

S_{cw} source term for water vapour generation at the cathode.

• Current density

$$i = i_0\left[\exp\left(\frac{\alpha_a F}{RT}\eta\right)-\exp\left(\frac{-\alpha_c F}{RT}\eta\right)\right] \tag{10}$$

i_0 [A/m^2] the exchange current density.

α_a and α_c are the anodic and cathodic charge transfer coefficients.

F [C/mol] is the Faraday constant.

R [J/mol·K] is the universal gas constant.

η is the overpotential (V), which is the difference between the actual electrode potential and the equilibrium potential.

• Total mass sources

$$\begin{aligned} &(\text{anode}):\mathrm{S_m}=\mathrm{S_{H_2}}+\mathrm{S_{aw}} \\ &(\text{cathode}):\mathrm{S_m}=\mathrm{S_{O_2}}+\mathrm{S_{cw}} \end{aligned} \tag{11}$$

2.2 Geometry

The 3D geometry of the proposed PEMFC was created using SolidWorks (Figure 3). The design features an FFP with an active area of 5 × 5 = 25 cm^2. On the anode side, there is a serpentine design with a channel width of 2 mm, while the cathode side is a fractal design. Panel (a) displays the top section of the cathode side, while panel (b) displays the bottom section; panel (c) displays the entire cell. The dimensional parameters are presented in Table 3. The widths of the channels of consecutive generations are related according to Murray's law (2). The depth of the channels was taken as 1 mm according to technological restrictions.

Table 3. Dimensional geometric parameters of the PEMFC studied

Parameter	Value (mm)
Plate dimension (L × W)	50 × 50
Thickness (FFP)	3
Channel depth (flow field)	1
Channels width (Flow field)	4, 3.2, 2.5, 2, 1.5, 1.25, 1
Thickness GDL	0.3
Thickness CL	0.12
Thickness PEM	0.08

2.3 Meshing

The developed 3D FFP geometry was transferred to the ANSYS workbench Mesher to discretise the geometry into small computational elements (Figure 4). Due to the complex processes in PEMFC, the simulation requires a fine mesh with relatively small computation time to get a converged solution.

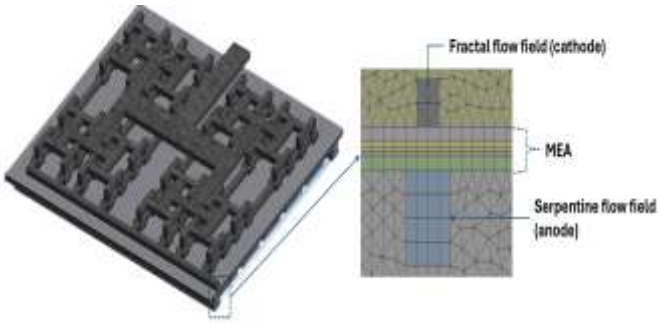

Figure 4. Mesh of the proposed FFP

A mesh independence assessment was performed using four mesh densities ranging from 0.9 to 2.7 million cells, as shown in Table 4. The difference in current density between 2.1 M and 2.7 M elements at 0.6 V was less than 0.06%, indicating that further refinement produces negligible variation in results. Therefore, the configuration with 2.7 million elements was selected for all simulations to ensure accuracy while maintaining reasonable computational cost.

To account for numerical uncertainty, discretization sensitivity was evaluated through the mesh refinement study presented above, and convergence criteria of 10^{-6} were applied for continuity, momentum, and species equations. Material properties were taken from standard PEMFC datasets provided within Fluent, introducing minor uncertainty related to transport coefficients. Considering these factors, the overall numerical uncertainty is expected to be low and suitable for comparative flow-field analysis.

Table 4. Mesh sensitivity test

Number of Elements	Current Density (w/m^2) at 0.6 V
900.000	0.611
1,500.000	0.60962
2,100.000	0.604593
2,700.000	0.604220

2.3 Boundary conditions

In this study, the boundary conditions for the 3D model of the PEMFC are defined in Tables 5 and 6 to ensure accurate simulation of the physical and electrochemical processes. The operating pressure, temperature, gas inlet conditions, and stoichiometric ratios used throughout the simulations are summarized in Table 5. The same operating conditions were applied to both configurations examined in this work (serpentine-serpentine/fractal-serpentine). The values presented in Table 6 correspond to different RH levels and were calculated using the FLUENT PEMFC calculator. These include the inlet mass flow rates of hydrogen, oxygen, and water vapor, adjusted for each RH condition to assess the impact of humidification on cell performance.

Table 5. Boundary conditions

Parameters	Value	Unit
Operating pressure	200 000	Pa
Operating temperature	353.15	K
Open-circuit voltage	1	V
Inlet hydrogen temperature	298.15	K
Inlet oxygen temperature	298.15	K
Stoichiometric factor of hydrogen (anode)	2	-
Stoichiometric factor of oxygen (cathode)	6	-

Table 6. Boundary conditions at different RH values

FFP	Anode (Serpentine)			Cathode (Fractal)		
Humidity level	Mass flow rate (kg/s)	H_2	H_2O	Mass flow rate (Kg/s)	O_2	H_2O
RH 50%	1.1437e-06	0.4530422	0.5469578	5.7836e-05	0.2150084	0.07725582
RH 55%	1.12156e-06	0.4262417	0.5737583	5.835e-05	0.2131157	0.08537863
RH 60%	1.2895e-06	0.4018162	0.5981838	5.8877e-05	0.2112052	0.09357773
RH 70%	1.4436e-06	0.3589304	0.6410696	5.9978e-05	0.6924609	0.1102092
RH 80%	1.6066e-06	0.3225012	0.6774988	6.1143e-05	0.2033804	0.127159

3. RESULTS AND DISCUSSION

The performance of the proposed PEMFC with the fractal FFP was evaluated and compared to the conventional serpentine design under identical operating conditions. The parameters used for both configurations are listed in Tables 5 and 6 across varying RH levels. The main results are summarized as follows.

3.1 Model validation

The numerical model was referenced to the experimental study of Sauermoser et al. [28], who reported that fractal PEMFCs operate most stably in the range of 60–70% relative humidity (RH). Figure 5 illustrates the measured voltage–time curves at RH = 50%, 60% and 70%, demonstrating that 70% RH provides the most stable output with minimal voltage decay over time. Based on this trend, RH = 70% was selected as the reference operating condition for validating the

numerical setup and for subsequent performance comparison.

3.2 Concentration of oxygen

The amount of current generation in a PEMFC is directly influenced by the oxygen concentration at the CL on the cathode side. Figure 6 shows the molar concentration contours of O_2 at the GDL/CL interface for both configurations: (a) the fractal FFP and (b) the serpentine FFP.

As illustrated in Figure 6(a), the fractal flow field provides more uniform and higher oxygen concentrations across the entire active area, with values reaching up to 2.16×10^{-2} kmol/m³ from the inlet to the outlet. This uniformity is due to the symmetrical and distributed branching structure of the fractal channels, which promotes balanced oxidant delivery throughout the electrode surface. In contrast, Figure 6(b) reveals that the serpentine FFP exhibits non-uniform oxygen distribution, with a maximum concentration of only 1.37×10^{-2} kmol/m³ near the inlet, followed by a gradual decline toward the outlet at 1.45×10^{-2} kmol/m³. This leads to reactant starvation at downstream sections, resulting in localized current density variations and potentially non-uniform electrochemical reactions and thermal gradients, which can accelerate membrane degradation. These findings confirm the superior reactant distribution performance of the proposed fractal FFP and align with trends reported in prior numerical studies [17, 19-23].

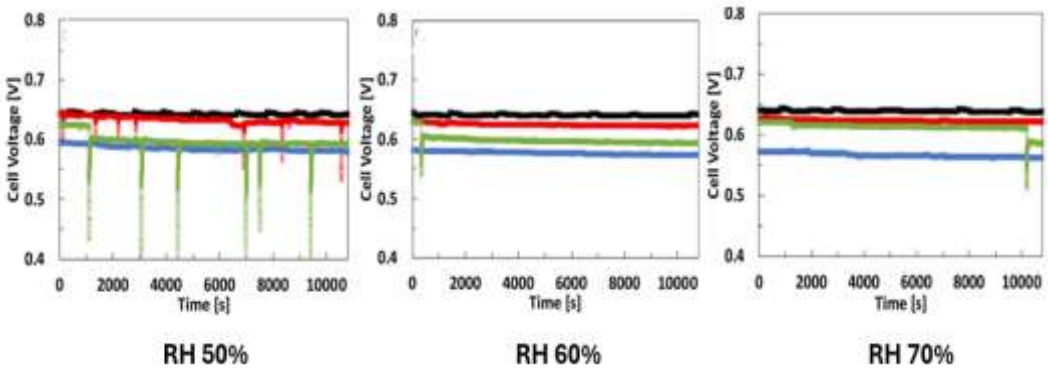

Figure 5. Operating voltage at RH = 50% (a), 60% (b), 70% (c) of fractal FFP [28]

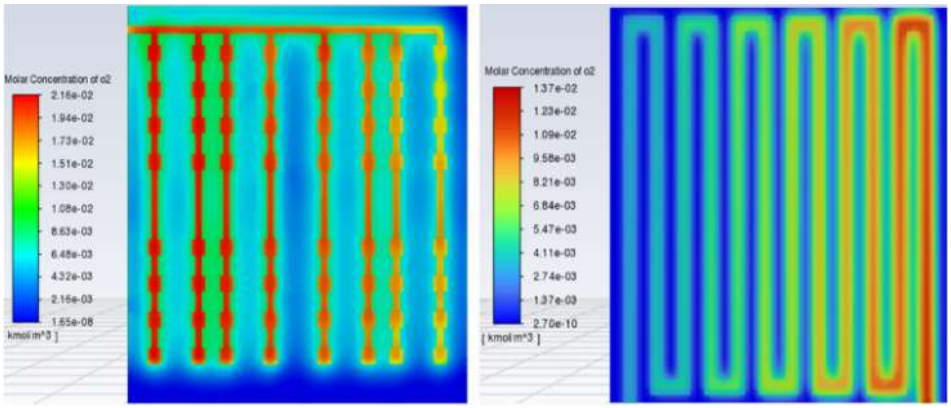

Figure 6. Molar concentration of O_2 at the cathode GDL/CL interface in the fractal (a) and serpentine (b) FFPs

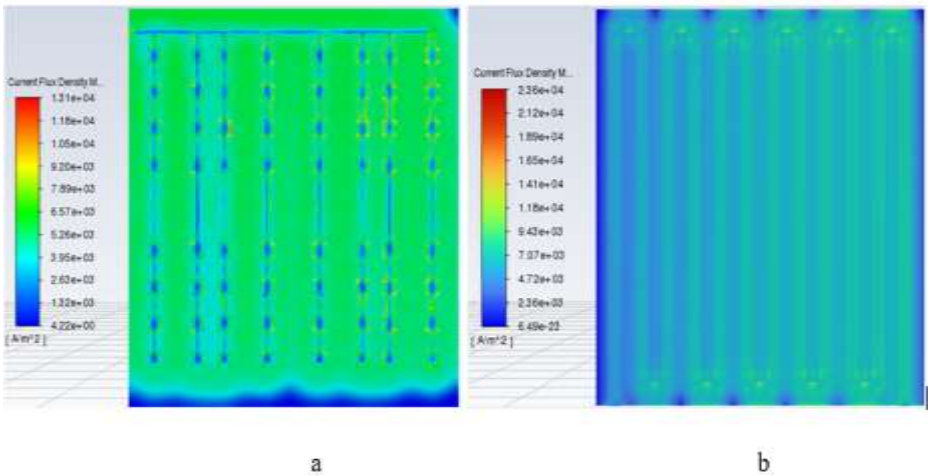

Figure 7. Current density at 0.6 V at the cathode GDL/CL interface of fractal (a) and serpentine (b) FFPs

3.3 Current density

The contours of current density and heat generation at the cathode CL interface are shown in Figures 7 and 8, based on CFD results under identical operating conditions. These distributions are crucial for evaluating the electrochemical performance and thermal management of the FC.

Figure 7 presents the current density distribution. In the case of the fractal FFP (Figure 7(a)), the current density reaches up to 1.31×10^4 A/m², especially concentrated at the outlets of the fractal branches, where oxygen is effectively delivered. The distribution is more uniform across the active area, reflecting improved oxygen availability and reactant utilization. In contrast, the serpentine FFP (Figure 7(b)) exhibits a lower peak current density of approximately 7.07×10^3 A/m², with weaker activity toward the outlet, indicating oxygen depletion and less efficient electrochemical performance.

Figure 8 presents the associated heat source distribution, which is primarily governed by the rate of electrochemical reaction. The fractal FFP (Figure 8(a)) shows a smoother and more balanced heat profile, consistent with the uniform current generation. Meanwhile, the serpentine FFP (Figure 8(b)) exhibits a highly non-uniform heat source pattern with concentrated hot spots, especially near the inlet, where reactant delivery is strongest. These differences imply that the serpentine FFP leads to higher local energy dissipation and entropy generation, potentially causing thermal stress and long-term degradation of the membrane. In contrast, the fractal design enhances thermal uniformity, which supports better durability and performance stability, as also supported by previous studies [13, 28, 38].

The higher heat generation observed near the inlet region in the serpentine plate is associated with local reactant availability and higher current density, which increases activation losses and ohmic heating. In contrast, the fractal configuration distributes oxygen more evenly across the cathode surface, leading to a more uniform reaction rate and lower localized heat peaks. This mitigates thermal gradients within the MEA, reducing the risk of membrane drying near the inlet and water condensation downstream.

3.4 Water mass fraction and water content

The distributions of water mass fraction and water activity at the cathode GDL/CL interface for the fractal FFP at Vcell = 0.6 V are illustrated in Figure 9(a) and (b).

The water mass fraction (Figure 9(a)) exhibits a gradual increase from the inlet toward the outlet, indicating effective water transport along the flow channels. The maximum water mass fraction reaches 6.56×10^{-2}, while maintaining a relatively balanced distribution across the active area. This uniformity is essential for mitigating localized flooding and ensuring stable reactant transport.

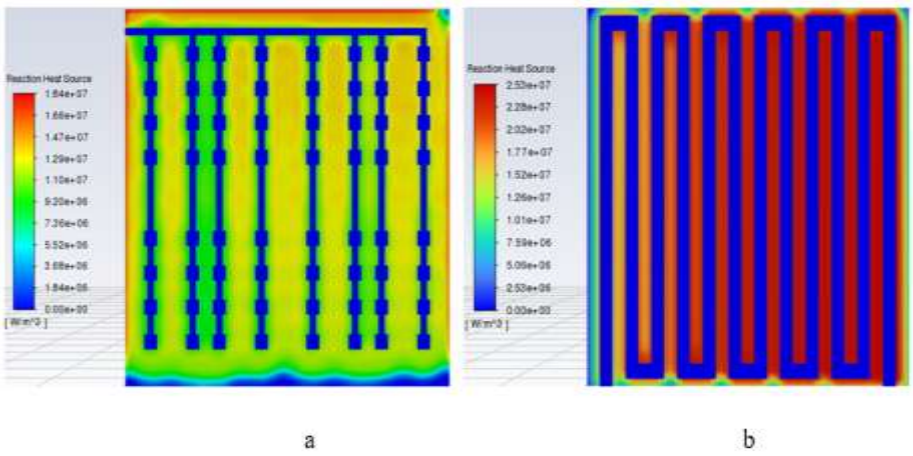

Figure 8. Heat source reaction 0.6 V at the cathode GDL/CL interface of (a) fractal, (b) serpentine

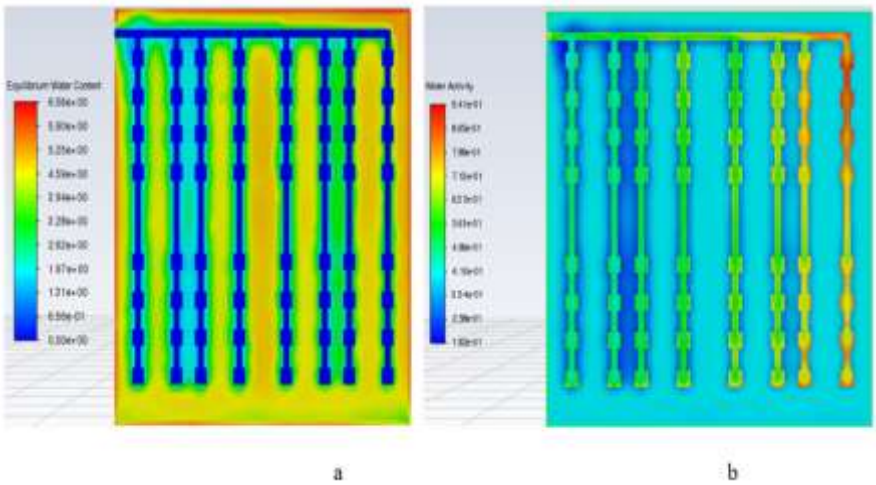

Figure 9. Water content (a) and water activity, (b) at the cathode GDL/CL interface

The water activity (Figure 9(b)) shows consistent hydration across most of the active area, with values ranging from 3.2 × 10^{-1} near the inlet to 9.4 × 10^{-1} near the outlet. However, a notable observation is the higher water activity at the corner opposite the outlet, which suggests a tendency for localized water accumulation in this region. This could lead to flooding under high-humidity operating conditions, potentially hindering reactant transport and reducing performance.

3.5 Performance and power curves

Figure 10 presents the power density curves for the fractal FFP under varying humidity levels: RH = 50%, 55%, 60%, 70% and 80%. The results indicate that the highest performance is achieved at 70% humidity when the maximum power density was 0.584 W/m^2, while a humidity level of RH = 80% marks the onset of performance decline. Figure 11 depicts a comparative analysis between the fractal and serpentine FFPs. The results demonstrate that the fractal design outperforms the serpentine design, showing an enhanced performance of 8%.

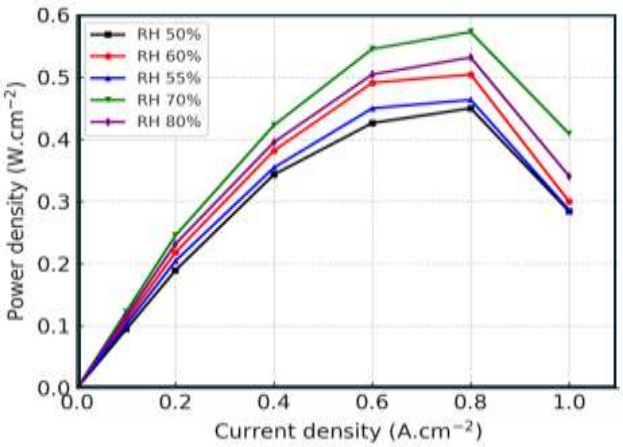

Figure 10. The power-current density curves in the case of fractal FFP at different RH

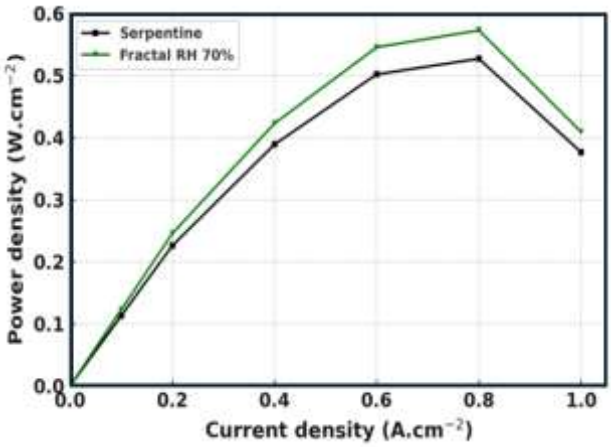

Figure 11. The comparison power density of the proposed fractal and standard serpentine FFP

The comparison across different operating humidities (50–80% RH) indicates a clear performance trend: power density increases with membrane hydration up to 70% RH, beyond which excess liquid water accumulation hinders oxygen transport and reduces cell output. These results confirm that 70% RH represents the optimal balance between proton conductivity and liquid water removal for the present fractal configuration.

3.6 Recommendations and propositions

3.6.1 Water management

Based on the obtained results (Figure 9), the current design leads to inefficient removal of excess water, which potentially results in flooding of the FFP channels. This section outlines two proposed design modifications aimed at addressing this issue.

The first proposition (Figure 12) is redesigning the water outlet position. An enhanced removal of excess water can be achieved by placing these outlets at the lowest points of the cell, which is consistent with recent studies highlighting the importance of outlet positioning in mitigating flooding [44]. The proposition (a) shows two outlets, while the proposition (b) suggests positioning a central outlet along the parallel channels for more efficient design.

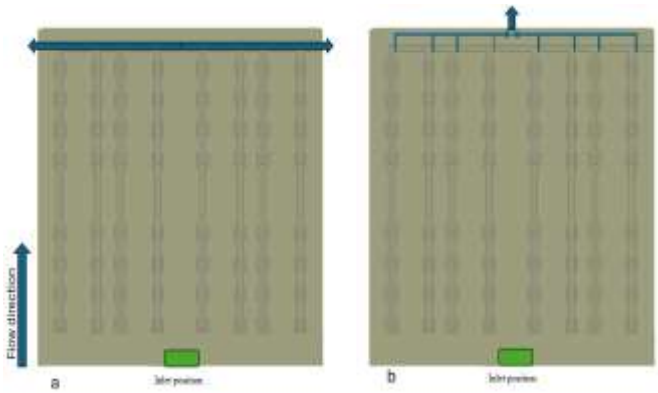

Figure 12. Proposed water outlet designs with one outlet, and two (a) or one (b) outlets for fractal PEMFC

The second proposition (Figure 13) is the integration of microgrooves in the flow channels, which is an innovative approach to improve water management in PEMFC, in line with recent findings that emphasize the synergy between flow field geometries and microporous structures for efficient liquid water removal [45]. The challenge of this proposition requires high precision, which means an increase in the cost and time of production of the FC [46]. Similar conclusions have been drawn in recent works, where structured flow field modifications showed potential for enhanced drainage but also raised concerns of increased design complexity [47].

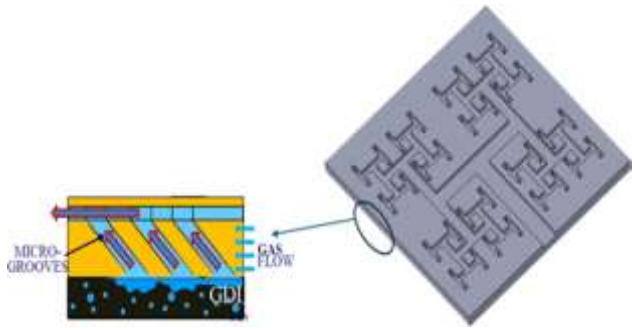

Figure 13. Proposed microgrooves for water removal from the FFP and GDL [46]

3.6.2 Uniform distribution of reactants

Fractal design generally promotes uniform reactant distribution through multi-branching; however, simulation results show that the 7th-generation configuration exhibits maldistribution near the terminal outlets, where channels become closely spaced due to the applied scaling factor. This reduced spacing decreases local pressure gradients and creates preferential flow pathways, preventing homogeneous access to end branches and lowering overall distribution uniformity.

To address this limitation, a 6-generation fractal architecture is recommended. Reducing one branching level restores more uniform outlet spacing and equalizes hydraulic resistance across branches (Figure 14), improving flow allocation while also reducing geometric complexity and fabrication effort. This confirms that increasing generations beyond an optimal point, especially under a narrower scaling factor, does not enhance uniformity, and an intermediate order provides a more balanced transport network for PEMFC operation.

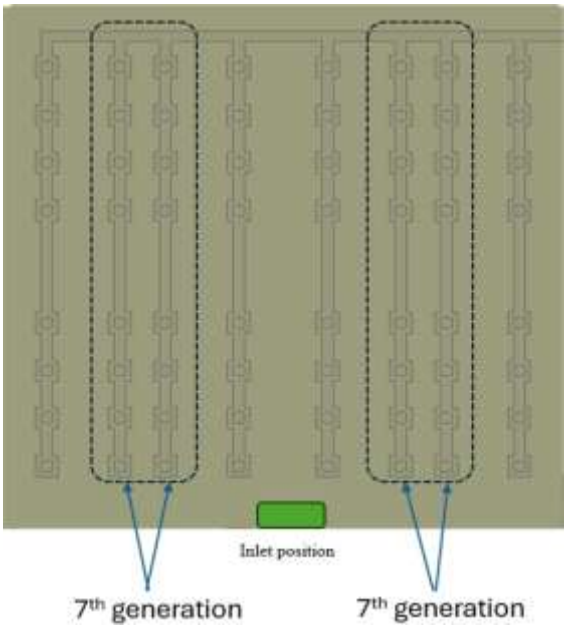

Figure 14. Distribution uniformity proposition

4. CONCLUSIONS

The results of this study demonstrated that the proposed T-junction fractal FFP achieves the best performance at a RH of 70%, showing an 8% increase in power density compared to a conventional serpentine FFP. This improvement is attributed to the more uniform oxygen distribution, effective water removal, and enhanced current density uniformity enabled by the fractal geometry. The introduction and verification of a new width scaling approach across the fractal generations played a key role in achieving these improvements.

Although the 7th-generation design showed the highest uniformity, the 6th generation is recommended based on the optimized scaling factor, which balances performance with improved uniformity, outlet alignment, and fabrication feasibility. The reduced-thickness structure also simplifies the manufacturing process compared to traditional 3D fractal plates. Additionally, this study contributes to the field by visualizing internal water transport behaviour in fractal geometries, an aspect often overlooked in prior works. Future work will focus on the experimental validation of the scaling methodology, the effect of generation number, and the water removal performance of the proposed designs.

In practical terms, the reduced-thickness fractal plate can support more compact and cost-efficient PEMFC stacks, making it suitable for portable energy devices, small vehicles, drones, and low-temperature hydrogen systems where water management and uniform reactant supply are critical. Its manufacturability also enables implementation through CNC machining or emerging low-cost fabrication routes, allowing the design to move toward prototyping and industrial use.

ACKNOWLEDGMENT

This research was conducted as part of the ENERGYTECHDEMO project under the Excellence Initiative: Research University (IDUB) programme, coordinated by POB Energy at Warsaw University of Technology.

REFERENCES

[1] Haider, R., Wen, Y., Ma, Z.F., Wilkinson, D.P., et al. (2021). High temperature Proton Exchange Membrane Fuel Cells: Progress in advanced materials and key technologies. Chemical Society Reviews, 50(2): 1138-1187. https://doi.org/10.1039/D0CS00296H

[2] Olabi, A.G., Wilberforce, T., Abdelkareem, M.A. (2021). Fuel cell application in the automotive industry and future perspective. Energy, 214: 118955. https://doi.org/10.1016/j.energy.2020.118955

[3] Qu, E., Hao, X., Xiao, M., Han, D., et al. (2022). Proton exchange membranes for high temperature Proton Exchange Membrane Fuel Cells: Challenges and perspectives. Journal of Power Sources, 533: 231386. https://doi.org/10.1016/j.jpowsour.2022.231386

[4] Wu, D., Peng, C., Yin, C., Tang, H. (2020). Review of system integration and control of Proton Exchange Membrane Fuel Cells. Electrochemical Energy Reviews, 3(3): 466-505. https://doi.org/10.1007/s41918-020-00068-1

[5] Cruz-Martínez, H., Tellez-Cruz, M.M., Guerrero-Gutiérrez, O.X., Ramírez-Herrera, C.A., Salinas-Juárez, M.G., Velázquez-Osorio, A., Solorza-Feria, O. (2019). Mexican contributions for the improvement of electrocatalytic properties for the oxygen reduction reaction in PEM fuel cells. International Journal of Hydrogen Energy, 44(24): 12477-12491. https://doi.org/10.1016/j.ijhydene.2018.05.168

[6] Chowdhury, M.Z., Genc, O., Toros, S. (2018). Numerical optimization of channel to land width ratio for PEM fuel cell. International Journal of Hydrogen Energy, 43(23): 10798-10809. https://doi.org/10.1016/j.ijhydene.2017.12.149

[7] Pollet, B.G., Kocha, S.S., Staffell, I. (2019). Current status of automotive fuel cells for sustainable transport. Current Opinion in Electrochemistry, 16: 90-95. https://doi.org/10.1016/j.coelec.2019.04.021

[8] Wilberforce, T., Amiri, A. (2023). Comparative study on bipolar plate geometry designs on the performance of Proton Exchange Membrane Fuel Cells. Fuel, 346: 128389. https://doi.org/10.1016/j.fuel.2023.128389

[9] Zhang, J., Huang, P., Ding, H., Xin, D., Sun, S. (2023). Investigation of the three-dimensional flow field for Proton Exchange Membrane Fuel Cell with additive manufactured stainless steel bipolar plates: Numerical simulation and experiments. Energy, 269: 126709. https://doi.org/10.1016/j.energy.2023.126709

[10] Xiong, K., Wu, W., Wang, S., Zhang, L. (2021). Modeling, design, materials and fabrication of bipolar plates for Proton Exchange Membrane Fuel Cell: A review. Applied energy, 301: 117443. https://doi.org/10.1016/j.apenergy.2021.117443

[11] Fan, W., Zhao, T., Jiang, K., Sun, L., et al. (2022). Plant vs. animal prototype for designing bio-inspired PEMFC flow fields: Corn veins or Murray's Law? Journal of Bionic Engineering, 19(3): 761-776. https://doi.org/10.1007/s42235-022-00174-4

[12] Sauermoser, M., Kizilova, N., Pollet, B.G., Kjelstrup, S. (2020). Flow field patterns for Proton Exchange Membrane Fuel Cells. Frontiers in Energy Research, 8: 13. https://doi.org/10.3389/fenrg.2020.00013

[13] Pedram, S., Batool, M., Yapp, K., Bonville, L., Jankovic, J. (2021). A review on bioinspired Proton Exchange Membrane Fuel Cell: Design and materials. Advanced Energy and Sustainability Research, 2(7): 2000092. https://doi.org/10.1002/aesr.202000092

[14] Shen, J., Tu, Z., Chan, S.H. (2020). Evaluation criterion of different flow field patterns in a Proton Exchange Membrane Fuel Cell. Energy Conversion and Management, 213: 112841. https://doi.org/10.1016/j.enconman.2020.112841

[15] Xie, Q., Zheng, M. (2021). CFD simulation and performance investigation on a novel bionic spider-web-type flow field for PEM fuel cells. Processes, 9(9): 1526. https://doi.org/10.3390/pr9091526

[16] Wang, Y., Si, C., Qin, Y., Wang, X., Fan, Y., Gao, Y. (2021). Bio-inspired design of an auxiliary fishbone-shaped cathode flow field pattern for polymer electrolyte membrane fuel cells. Energy Conversion and Management, 227: 113588. https://doi.org/10.1016/j.enconman.2020.113588

[17] Xia, L., Yu, Z., Xu, G., Ji, S., Sun, B. (2021). Design and optimization of a novel composite bionic flow field structure using three-dimensional multiphase computational fluid dynamic method for Proton Exchange Membrane Fuel Cell. Energy Conversion and Management, 247: 114707. https://doi.org/10.1016/j.enconman.2021.114707

[18] Liu, S., Chen, T., Xie, Y., Zhang, J., Wu, C. (2019). Numerical simulation and experimental study on the effect of symmetric and asymmetric bionic flow channels on PEMFC performance under gravity. International Journal of Hydrogen Energy, 44(56): 29618-29630. https://doi.org/10.1016/j.ijhydene.2019.06.046

[19] Guo, N., Leu, M.C., Koylu, U.O. (2014). Bio-inspired flow field designs for polymer electrolyte membrane fuel cells. International Journal of Hydrogen Energy, 39(36): 21185-21195. https://doi.org/10.1016/j.ijhydene.2014.10.069

[20] Roshandel, R., Arbabi, F., Moghaddam, G.K. (2012). Simulation of an innovative flow-field design based on a bio inspired pattern for PEM fuel cells. Renewable Energy, 41: 86-95. https://doi.org/10.1016/j.renene.2011.10.008

[21] Kang, H.C., Jum, K.M., Sohn, Y.J. (2019). Performance of unit PEM fuel cells with a leaf-vein-simulating flow field-patterned bipolar plate. International Journal of Hydrogen Energy, 44(43): 24036-24042. https://doi.org/10.1016/j.ijhydene.2019.07.120

[22] Asadzade, M., Shamloo, A. (2017). Design and simulation of a novel bipolar plate based on lung-shaped bio-inspired flow pattern for PEM fuel cell. International Journal of Energy Research, 41(12): 1730-1739. https://doi.org/10.1002/er.3741

[23] Bethapudi, V.S., Hack, J., Trogadas, P., Cho, J.I.S., Rasha, L., Hinds, G., Coppens, M.O. (2019). A lung-inspired printed circuit board polymer electrolyte fuel cell. Energy Conversion and Management, 202: 112198. https://doi.org/10.1016/j.enconman.2019.112198

[24] Trogadas, P., Cho, J.I.S., Neville, T.P., Marquis, J., Wu, B., Brett, D.J.L., Coppens, M.O. (2018). A lung-inspired approach to scalable and robust fuel cell design. Energy & Environmental Science, 11(1): 136-143. https://doi.org/10.1039/C7EE02161E

[25] Badduri, S.R., Srinivasulu, G.N., Rao, S.S. (2020). Influence of bio-inspired flow channel designs on the performance of a PEM fuel cell. Chinese Journal of Chemical Engineering, 28(3): 824-831. https://doi.org/10.1016/j.cjche.2019.07.010

[26] Behrou, R., Pizzolato, A., Forner-Cuenca, A. (2019). Topology optimization as a powerful tool to design advanced PEMFCs flow fields. International Journal of Heat and Mass Transfer, 135: 72-92. https://doi.org/10.1016/j.ijheatmasstransfer.2019.01.050

[27] Lorenzini-Gutierrez, D., Hernandez-Guerrero, A., Ramos-Alvarado, B., Perez-Raya, I., Alatorre-Ordaz, A. (2013). Performance analysis of a Proton Exchange Membrane Fuel Cell using tree-shaped designs for flow distribution. International Journal of Hydrogen Energy, 38(34): 14750-14763. https://doi.org/10.1016/j.ijhydene.2013.08.012

[28] Sauermoser, M., Pollet, B.G., Kizilova, N., Kjelstrup, S. (2021). Scaling factors for channel width variations in tree-like flow field patterns for polymer electrolyte membrane fuel cells-An experimental study. International Journal of Hydrogen Energy, 46(37): 19554-19568. https://doi.org/10.1016/j.ijhydene.2021.03.102

[29] Ghadhban, S.A., Alawee, W.H., Dhahad, H.A. (2021). Study effects of bio-inspired flow filed design on polymer electrolyte membrane fuel cell performance. Case Studies in Thermal Engineering, 24: 100841. https://doi.org/10.1016/j.csite.2021.100841

[30] Jang, J.Y., Cheng, C.H., Liao, W.T., Huang, Y.X., Tsai, Y.C. (2012). Experimental and numerical study of Proton Exchange Membrane Fuel Cell with spiral flow channels. Applied Energy, 99: 67-79. https://doi.org/10.1016/j.apenergy.2012.04.011

[31] Li, N., Wang, W., Xu, R., Zhang, J., Xu, H. (2023). Design of a novel nautilus bionic flow field for Proton Exchange Membrane Fuel Cell by analyzing performance. International Journal of Heat and Mass Transfer, 200: 123517. https://doi.org/10.1016/j.ijheatmasstransfer.2022.123517

[32] Huang, H., Li, X., Li, S., Guo, X., Liu, M., Wang, T., Lei, H. (2023). Evaluating the effect of refined flow channels in a developed biomimetic flow field on PEMFC performance. Energy, 266: 126442.

https://doi.org/10.1016/j.energy.2022.126442
[33] Shen, J., Tu, Z., Chan, S.H. (2020). Performance enhancement in a Proton Exchange Membrane Fuel Cell with a novel 3D flow field. Applied Thermal Engineering, 164: 114464. https://doi.org/10.1016/j.applthermaleng.2019.114464
[34] Murray, C.D. (1926). The physiological principle of minimum work: I. The vascular system and the cost of blood volume. Proceedings of the National Academy of Sciences, 12(3): 207-214. https://doi.org/10.1073/pnas.12.3.207
[35] Weibel, E.R., Cournand, A.F., Richards, D.W. (1963). Morphometry of the Human Lung (Vol. 1). Berlin: Springer.
[36] Kizilova, N. (2004). Computational approach to optimal transport network construction in biomechanics. In International Conference on Computational Science and its Applications, pp. 476-485. https://doi.org/10.1007/978-3-540-24709-8_51
[37] LaBarbera, M. (1990). Principles of design of fluid transport systems in zoology. Science, 249(4972): 992-1000. https://doi.org/10.1126/science.2396104
[38] Uylings, H.B.M. (1977). Optimization of diameters and bifurcation angles in lung and vascular tree structures. Bulletin of Mathematical Biology, 39(5): 509-520. https://doi.org/10.1016/S0092-8240(77)80054-2
[39] Sauermoser M, Kjelstrup S., Kizilova N., Pollet B.G., Flekkoy E.G. (2020) Seeking minimum entropy production for a tree-like flow-field in a fuel cell. Physical Chemistry & Chemical Physics, 22(13): 6993-7003. https://doi.org/10.1039/C9CP05394H
[40] Bethapudi, V.S., Hack, J., Hinds, G., Shearing, P.R., Brett, D.J.L., Coppens, M.O. (2021). Electro-thermal mapping of polymer electrolyte membrane fuel cells with a fractal flow-field. Energy Conversion and Management, 250: 114924. https://doi.org/10.1016/j.enconman.2021.114924
[41] ANSYS, ANSYS Fluent Fuel Cell Module Manual. 2017.
[42] Heidary, H., Kermani, M.J., Prasad, A.K., Advani, S.G., Dabir, B. (2017). Numerical modelling of in-line and staggered blockages in parallel flowfield channels of PEM fuel cells. International Journal of Hydrogen Energy, 42(4): 2265-2277. https://doi.org/10.1016/j.ijhydene.2016.10.076
[43] Dhanasekaran, A., Subramanian, Y., Omeiza, L.A., Raj, V., Yassin, H.P.H.M., Sa, M.A., Azad, A.K. (2022). Computational fluid dynamics for Protonic Ceramic Fuel Cell stack modeling: A brief review. Energies, 16(1): 208. https://doi.org/10.3390/en16010208
[44] Shi, C., Yin, C., Luo, W., Liu, H., Tang, H. (2025). Study of current distribution generation in PEMFC based on conditional variational auto-encoder. Energy and AI, 21: 100568. https://doi.org/10.1016/j.egyai.2025.100568
[45] Pan, Z., Wu, L., Xie, F., Zhang, Z., Zhao, Z., Esan, O.C., Zhang, X. Chen, R., An, L. (2024). Engineered wettability-gradient porous structure enabling efficient water manipulation in regenerative fuel cells. Energy and AI, 17: 100400. https://doi.org/10.1016/j.egyai.2024.100400
[46] Utaka, Y., Koresawa, R. (2016). Performance enhancement of polymer electrolyte fuel cells by combining liquid removal mechanisms of a gas diffusion layer with wettability distribution and a gas channel with microgrooves. Journal of Power Sources, 323: 37-43. https://doi.org/10.1016/j.jpowsour.2016.05.036
[47] Zhao, Y., Liu, Z., Huang, R., Wang, L., Chen, Y. (2025). Advances in flow-field structural modifications for enhanced water removal in PEM fuel cells. Energy AI, 16: 100568.